$NaFe_3(HPO_3)_2((H,F)PO_2OH)_6$: a potential cathode material and a novel ferrimagnet

Irene Munaò[1], Elena A. Zvereva[2], Olga S. Volkova[2,3,4], Alexander N. Vasiliev[2,3,4,#], A. Robert Armstrong[1] and Philip Lightfoot[1,*]

[1]School of Chemistry, University of St Andrews, St Andrews, Fife KY16 9ST, UK
[2]Faculty of Physics, Moscow State University, 119991 Moscow, Russia
[3]Theoretical Physics and Applied Mathematics Department, Ural Federal University, 620002 Ekaterinburg, Russia
[4]National University of Science and Technology "MISiS", Moscow 119049, Russia

A novel iron fluoro-phosphite, $NaFe_3(HPO_3)_2((H,F)PO_2OH)_6$, has been synthesized by a dry low temperature synthesis route. The phase has been shown to be electrochemically active for reversible intercalation of Na^+ ions, with an average discharge voltage of 2.5 V and an experimental capacity at low rates of up to 90 mAh/g. Simple synthesis, low cost materials, excellent capacity retention and efficiency suggest this class of material is competitive with similar oxyanion-based compounds as a cathode material for Na-batteries. The characterization of physical properties by means of magnetization, specific heat and electron spin resonance measurements confirms the presence of two magnetically non-equivalent Fe^{3+} sites. The compound orders magnetically at $T_C \sim 9.4$ K into a state with spontaneous magnetization.

Introduction

The ever-growing demand for portable energy has driven the search for new electrode materials for rechargeable battery applications. Lithium-ion batteries have so far been preferred to their sodium-ion counterparts for their higher energy density and operating voltages, leading to their domination of the portable electronics market and making them the best candidate for electric vehicles[1], but concerns about lithium supply and its rising cost have encouraged the scientific community to turn its attention to the more sustainable sodium-ion batteries.[1-7] The resurgence of interest in sodium-ion batteries has been driven by the greater and more uniform Earth abundance of sodium, compared with lithium, and hence potentially lower cost. Sodium-ion batteries could be major players in next-generation low-carbon energy technologies and in the promotion of sustainable global economic growth. The demand for large scale batteries to store the electricity from solar cells, wind turbines and other renewable sources has increased. The larger mass of sodium, compared with lithium, leads to a lower specific capacity for sodium cells, compared to corresponding lithium equivalents, but this is no disadvantage for static applications such as grid storage. Due to the low cost, the availability and the abundance of sodium, the interest in the synthesis of electrodes based on sodium has increased, especially using hydrothermal methods.[8]

Several electrode materials with high energy density have been reported for sodium batteries. Due to the similarity in the operation of lithium and sodium ion batteries, sodium

equivalents of the lithium based electrode materials, such as hard carbon, phosphates, pyrophosphates and oxides, have been described.[8-10] Layered oxides, AMO_2, where A = Li, Na and M is one or more transition metals, exhibit very different behavior depending on the alkali ion. For example, electrochemically inactive $LiFeO_2$ and $LiCrO_2$ behave well in their sodium forms, $NaFeO_2$ and $NaCrO_2$, due to the accessibility of the Fe^{4+} and Cr^{4+} states when A = Na.[11,12] Since the main market for Na-ion batteries is in grid-scale storage, where cost is of paramount importance, attention is focused on sodium cathodes based on low-cost, earth-abundant, transition metals such as Mn and Fe. Of the layered Na_xMnO_2 compounds, α-$NaMnO_2$, which exhibits a monoclinic distortion of the O3 crystal structure of $LiCoO_2$ (ABC oxygen stacking), and P2-$Na_{0.67}MnO_2$ (ABBA oxygen stacking), have demonstrated sodium deintercalation.[13-16] The reversibility of the deintercalation process in the P2 polymorph is enhanced by Mg doping.[17] Solid solutions of Mn and Fe, $Na_x[Mn_{1-y}Fe_y]O_2$, adopting either O3 or P2 structures, have also been investigated.[10,18]

Polyoxyanion compounds, particularly phosphates, are receiving considerable attention as alternative cathodes for rechargeable lithium and sodium batteries. The strong binding of the oxygen within polyoxyanions enhances stability and thus safety, compared with transition metal oxides. The electronic inductive effect shifts the d-states of the transition metal ions and hence the redox potentials, providing a means of tuning the latter.[8,19] In polyoxyanion compounds it is also possible to vary the iono-covalency of the metal−ligand bond in X−O−M (X = B, S, P, Si etc.; M = transition metal) linkage through the inductive effect of X by changing the electronegativity of the central atom, controlling the redox potential on the transition metal center.[20] In addition, polyanions are inclined to form two-dimensional (2-D) and three-dimensional (3-D) structures with different connectivity between the polyanion and the transition metals.[21] This has led to the synthesis of compounds of transition metals incorporating PO_4^{3-},[22,23] SO_4^{2-},[24,25] SiO_4^{4-},[26,27] BO_3^{3-},[28,29] mixed PO_4^{3-}, and CO_3^{2-}.[30,31] However, phosphite based compounds have not been studied in depth as battery materials. The only reported examples are $Li_{1.43}[Fe_{4.43}^{2+}Fe_{0.57}^{3+}(HPO_3)_6]\cdot 1.5H_2O$ with a specific capacity of 12 $mAh\cdot g^{-1}$,[32] showing very limited electrochemical activity and two materials with higher electrochemical activity, reported recently: $Li_3Fe_2(HPO_3)_3Cl$[33] and $LiFe(HPO_3)_2$,[34] each showing a specific capacity of ~70 $mAh\cdot g^{-1}$.

Due to these interesting results, we focused our attention on the synthesis and electrochemical activity of other possible phosphite-based compounds of iron. In this article, we report the synthesis and structural properties of a new sodium iron (III) fluoro-phosphite, $NaFe_3(HPO_3)_2((H,F)PO_2OH)_6$ (hereinafter abbreviated "**NaFP**") and demonstrate its electrochemical activity toward reversible insertion of Na^+ ions. This new phase exhibits close to theoretical capacity (99 $mAh\cdot g^{-1}$) at low rates and shows good capacity retention upon extended cycling.

Transition metal-containing polyanionic framework materials often show interesting magnetic properties. Therefore, we have also carried out a detailed investigation of the magnetism-related properties of **NaFP**. The preliminary results of these studies are presented

here, incorporating electron spin resonance, magnetization and specific heat measurements down to liquid helium temperatures.

Experimental Section

Material synthesis. **NaFP** was synthesized by reaction of NaF (1 mmol), Fe_2O_3 (1 mmol), H_3PO_3 (0.122 mmol). This mixture was sealed in a Teflon-lined stainless steel autoclave and heated to 140 °C for 3 days. The reaction was cooled to room temperature. Pink air-stable prismatic crystals were recovered by filtration from a minor aqueous phase.

Structural Characterization. Single crystal X-ray diffraction data were measured at 173 K on a Rigaku SCX Mini diffractometer using Mo Kα radiation (λ =0.71073 Å). Indexing and data processing were performed with Rigaku CrystalClear 2.0 and the structure was solved by direct methods and refined using the SHELX suite incorporated into the WinGX package. The material was found to adopt a triclinic structure in centrosymmetric space group, $P\bar{1}$ (Table 1). All non-H atoms were refined anisotropically. Initially, all H-atoms were located by Fourier methods and refined without constraints. However, it was apparent that two of the P-H moieties showed significantly enhanced electron density (1-2 e $Å^{-3}$) at the 'H' sites. These two H sites were therefore refined as partially occupied F sites. In order to verify the sample purity, a powder X-ray diffraction (PXRD) pattern was collected using a PANalytical Empyrean diffractometer in Bragg-Brentano geometry with Cu $K_{\alpha 1}$ radiation. Powder X-ray diffraction measurements on cycled electrodes were performed on a Stoe STADI/P diffractometer operating in capillary mode, with Fe$K\alpha_1$ radiation (λ = 1.936 Å) to eliminate Fe fluorescence. Samples were loaded in 0.5 mm glass capillaries and data were collected overnight. Scanning electron microscopy (SEM) was carried out on a JEOL JSM-5600 using an accelerating voltage of 5 kV. In order to confirm the incorporation of a small amount of fluoride, as suggested by the single crystal analysis, Energy-dispersive X-ray analysis (EDX) was carried out. Infra-red (IR) spectroscopy was carried out on a Shimadzu IRAffinity-1S, thermogravimetric analysis (TGA) on a Stanton Redcroft STA-780 series instrument.

Table 1: Crystallographic data for **NaFP**.

Molecular formula	$NaFe_3(HPO_3)_2((H_{0.93}F_{0.07})PO_2OH)_6$
Formula Mass (amu)	843.61
Crystal system	Triclinic
Space group	P -1
a	7.5302(4) Å
b	9.1696(3) Å
c	9.4732(11) Å
α	118.063 (5)°
β	101.274(12)°
γ	101.192(12)°

V (A^3)	534.25 (8)
Z	1
ρ (calcd) (g/cm^3)	2.622
Temp (K)	173 (2)
λ (Å)	0.71073 Å
F (000)	418.0
μ (mm^{-1})	2.747 (calculated)
θ_{max} (deg)	25.38
Index range	$-9 \le h \le 9$
	$-11 \le k \le 11$
	$-11 \le l \le 11$
R_{int}	0.0594
R_1/wR_2 ($I > 2\sigma$)	0.0272/0.0812
R_1/wR_2 (all data)	0.0284/0.0832
GOF on F_2	0.655
Largest diff peak and hole ($e/Å^{-3}$)	0.56/-0.55
Reflections number gt	1798
Reflections number total	1950

Electrochemical Characterization. The electrochemical performance of **NaFP** was evaluated at room temperature. Composite electrodes were prepared by mixing **NaFP**, super S carbon and Ketjen black carbon in the weight ratio 60:15:15 for 3.5 h using a Fritsch Pulverisette 7 mill followed by addition of Kynar Flex 2801 as binder dissolved in N-methyl-2-pyrrolidone (NMP). The slurry was then cast on aluminum foil using a doctor blade. The final ratio of the active material, conducting carbon and the binder in the electrodes was 60:30:10. Typical electrode active material loadings were 3-5 $mgcm^{-2}$. Electrodes were incorporated into coin cells (CR2325 type) with a sodium metal counter electrode, and with an electrolyte solution composed of 1M $NaClO_4$ in propylene carbonate containing 3% fluoroethylene carbonate as an additive. Electrochemical measurements were carried out at room temperature using a Biologic MacPile II system in the potential ranges1.5-4.2 V and 1.7-4 V at various C-rates.

The samples for *ex situ* measurements (PXRD) were prepared by extracting the cathode material from the coin cells and washing it with dry dimethyl carbonate (DMC). The solvent was then evaporated. All steps were performed in an Ar-filled glovebox. The resulting powder was stored in an Ar-filled glovebox for further characterization.

Physical Characterization. Magnetic dc-susceptibility measurements were performed at the magnetic field B = 0.1 T using a Quantum Design MPMS-7T system, and the specific heat measurements were carried out by a relaxation method using a Quantum Design PPMS-9T system in the temperature range 2 – 250 K. Electron spin resonance (ESR) studies were carried out using an X-band ESR spectrometer CMS 8400 (ADANI) ($f \approx 9.4$ GHz, $B \le 0.7$ T) equipped with a low-temperature mount, operating in the range $T = 6 – 300$

K. The main spectroscopic parameters are: microwave power 1 mW, magnetic field modulation frequency 100 kHz and amplitude 1 mT and spectral resolution 0.15 mT/pt. The effective g-factors of our samples have been calculated with respect to an external reference for the resonance field. We used BDPA (bisdiphenylene-b-phenylallyl) $g_{ref} = 2.00359$, as a reference material.

Results and Discussion

Crystal Structure. **NaFP** crystallises as well-faceted prismatic blocks with typical particle size about 200 μm, as shown in the SEM images (Fig. 1). Phase purity was confirmed by comparison of the experimental PXRD on the as-made material with a pattern simulated on the basis of this crystal structure (SI, Fig. S1). The EDX data (SI, Fig. S2), together with the single crystal analysis, suggest a small degree of fluoride incorporation. This was successfully modelled by the incorporation of $(FPO_2OH)^-$ groups substituting for $(HPO_2OH)^-$ groups at the P(2) and P(4)-containing polyhedra. The refinement suggests a final composition of approximately "$NaFe_3(HPO_3)_2((H_{0.93},F_{0.07})PO_2OH)_6$" For simplicity, we limit the following discussion to H-containing phosphite groups only, during the remainder of the paper. The presence of P-H groups was confirmed by IR (Fig. S3).

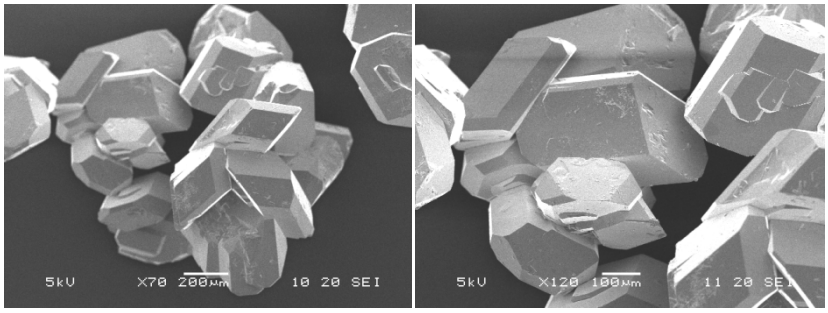

Fig. 1. SEM view of typical **NaFP** crystallites.

The crystal structure exhibits a novel 3-D framework with FeO_6 octahedra corner-sharing with HPO_3 and HPO_2OH tetrahedra, as shown in Fig. 2. This low-symmetry structure has two crystallographically distinct Fe sites (one on an inversion centre), four P sites and one Na site (on an inversion centre) in the asymmetric unit. Both Fe sites have octahedral coordination, with bond lengths in the normal range for Fe^{3+} (1.974 – 2.026 Å). Bond valence sum (BVS) calculations[35] were used to support both the Fe oxidation states and the location of the -OH groups. The bond valence parameters for the $(PH)^{4+}$ moiety were used[36.] There are no direct Fe-O-Fe linkages. Open channels run along all three principal directions, within which the Na^+ cations reside, being coordinated to six different HPO_2OH groups *via* the oxygen atoms of the P-O-H moieties.

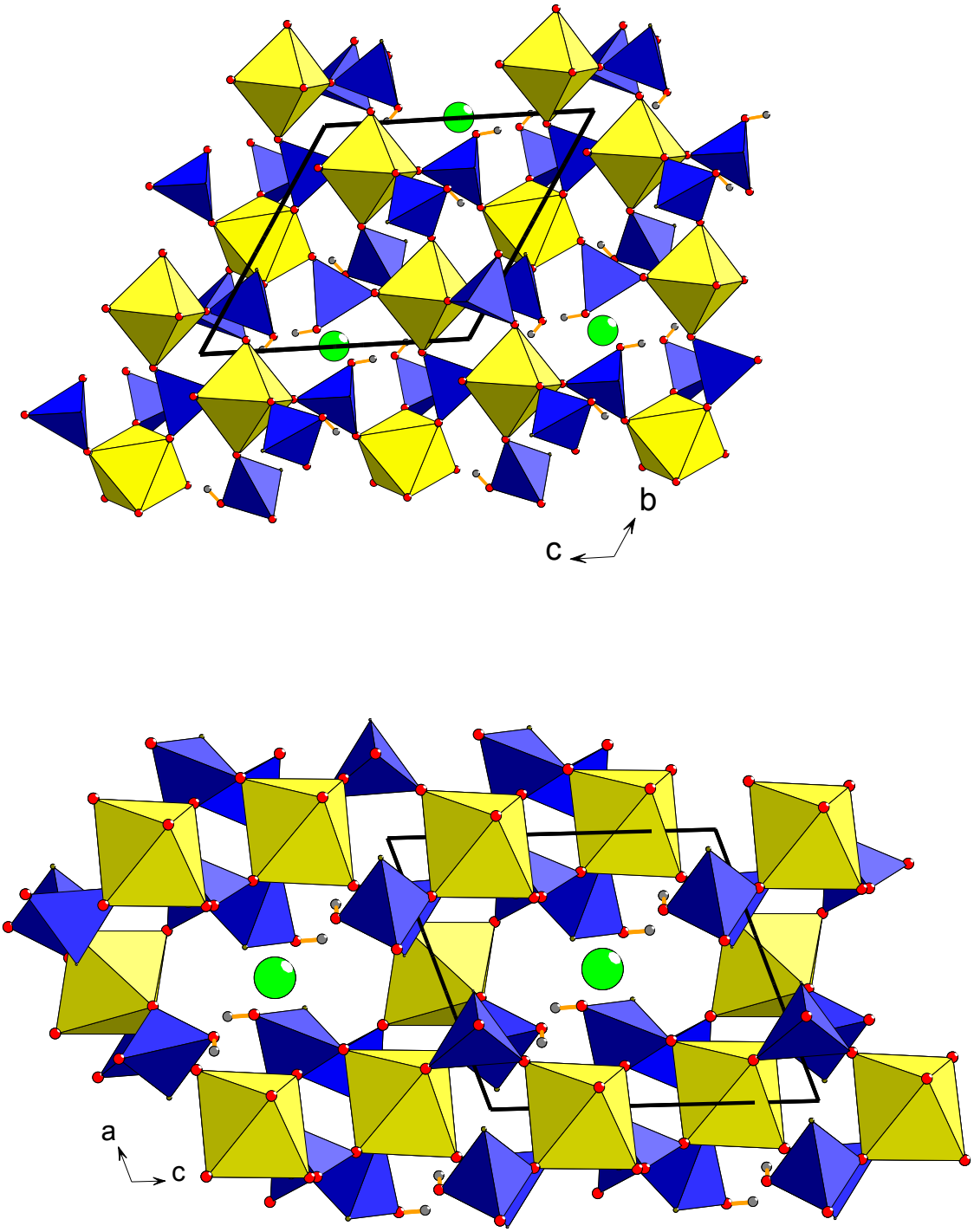

Fig. 2. Polyhedral representation of the crystal structure along the *a*-axis (a) and *b*-axis (b).

Viewed along the *a*-axis there are S-shaped eight-membered rings of alternating corner-shared Fe-centred octahedra and P-centred terahedra (Fig. 2(a)). Similar, odd-shaped 10-membered rings occur along the *b*-axis (Fig. 2(b)), and more regular eight-membered ring channels run along *c*. The net result is a complex and quite open framework, amenable to several distinct ionic migration pathways for Na^+. Selected bond lengths and bond valence sums are given in Table 2. Due to the complexity of the crystal structure, and in order to identify more easily the magnetic superexchange pathways, it is helpful to represent the structure in terms of key structural elements and also in terms of the framework connectivity of the Fe---P polyhedral units only, excluding oxygen ligands, and the near-neighbour Fe---Fe pathways. A key structural feature of the framework is a chain of $Fe(2)O_6$ octahedra linked *via* corners through bridging phosphite (P(3) and P(4)) groups (Fig. 3). These chains run along the [011] direction and are linked *via* P(1) and P(2) phosphite groups (Fig. 4). Fe---P distances are in the range 3.2 – 3.4 Å. Fe(2)---Fe(2) distances along the [011] chains alternate, with values of 4.82 and 4.94 Å; these are the shortest Fe---Fe interactions, with the shortest Fe(2)---Fe(1) and Fe(1)---Fe(1) distances being 5.62 and 7.53 Å, respectively. Taken together, the Fe(2)---Fe(1) superexchange network contains chains of corner- and edge-linked triangles extending in two directions (Fig. 5). The thermal robustness of the crystal structure is confirmed by TGA, which shows no weight loss until around 250° C (Fig. S4).

Table 2: Selected bond lengths and bond valence sums

		Bond length (Å)	**Bond valence**
Fe1	O3 x2	1.9884(18)	0.538
	O4 x2	1.9822(17)	0.547
	O8 x2	2.0259(18)	0.486
			∑ **3.142**
Fe2	O2	1.9948(18)	0.529
	O6	1.9744(19)	0.558
	O7	2.0210(18)	0.492
	O9	1.9883(18)	0.538
	O10	1.9953(18)	0.528
	O12	1.9778(18)	0.553
			∑ **3.198**
H2P1	O1	1.571(2)	1.160
	O2	1.4999(19)	1.406
	O3	1.5065(19)	1.381
			∑ **3.947**
H3P2	O4	1.4957(18)	1.452
	O5	1.574(2)	1.150
	O6	1.488(2)	1.452
			∑ **4.054**

H5P3	O7	1.5350(19)	1.279
	O8	1.5290(19)	1.300
	O9	1.5191(2)	1.335
			∑ **3.914**
H6P4	O10	1.4994(18)	1.408
	O11	1.576(2)	1.145
	O12	1.5022(19)	1.400
			∑ **3.953**
Na1	O1 x2	2.5022(19)	0.151
	O5 x2	2.349(2)	0.229
	O11x2	2.504(2)	0.151
			∑ **1.062**

$ P atoms have been treated as $(HP)^{4+}$ moieties; F atoms are not included – see text

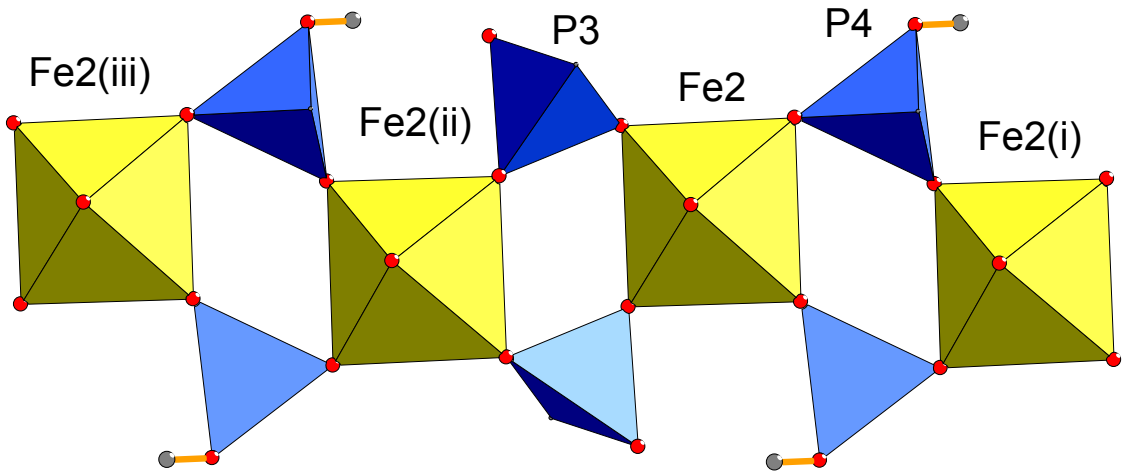

Fig. 3. Corner-linked Fe(2)-phosphite chain. Fe---Fe distances alternate: *via* P(3) bridge 4.82 Å, *via* P(4) bridge 4.94 Å.

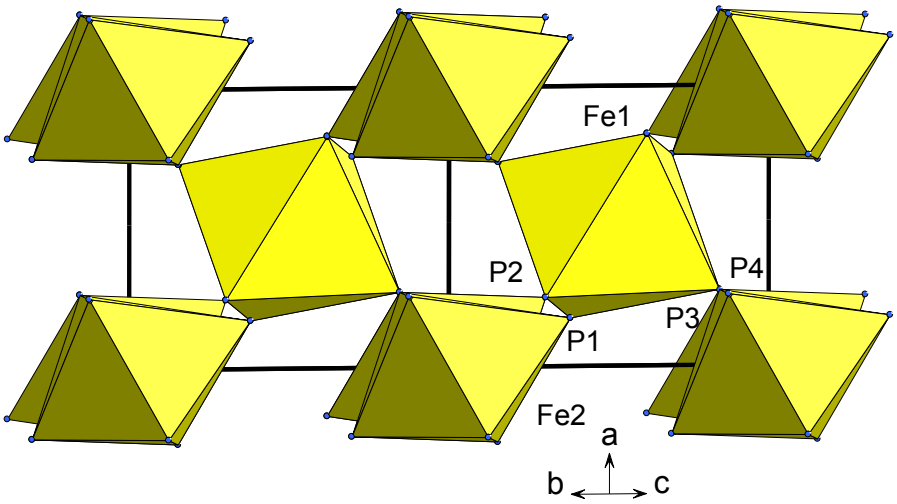

Fig. 4. Linkage of neighbouring Fe(2)-P chains *via* P(1)-Fe(1)-P(3) bridges. Note that oxygen atoms are omitted; the polyhedral vertices represent P atoms.

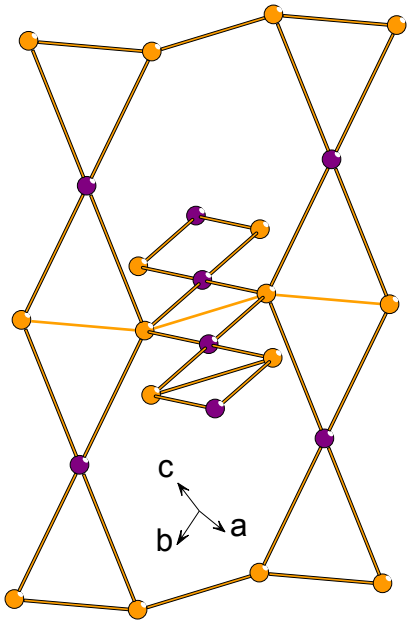

Fig. 5. Fe---Fe sublattice showing 'diamond-like' chains extending in two dimensions approximately perpendicular to the Fe(2)-P chains in Figures 3 and 4. Fe(2) sites orange, Fe(1) sites purple.

Electrochemistry. **NaFP** samples were incorporated into electrochemical cells as described in the experimental section. Load curves (corresponding to sodium insertion and extraction) at a rate of 10 mAg^{-1} (C/10) are presented for the voltage window 1.7 – 4.0 V (Fig. 6). Data collected over the wider voltage range of 1.5 – 4.2 V are shown in Fig. S5. The load curves show a sloping potential, suggesting solid solution behavior, with an average discharge voltage of around 2.5 V vs. Na^+/Na. The load curves are essentially invariant on cycling indicating good structural stability and reversibility. The material delivers close to theoretical capacity (99 $mAhg^{-1}$) over the wider voltage window, albeit with significant cell polarization. There are indications that some of the capacity delivered over the larger potential range has its origin in the conducting carbon additive[37]. This is highlighted by the first charge capacity exceeding the discharge, implying the formation of Fe (IV). The high polarization was observed at even very slow cycling rates (C/50) which, together with the need to add as much as 30% conductive carbon additive to achieve satisfactory performance, indicates rather poor electronic mobility in this compound. **NaFP** exhibits excellent capacity retention as shown in Fig. 7 and Fig. S6, together with Coulombic efficiencies of close to 100%. At higher charge/discharge rates (1C, 100 mAg^{-1}) there is little reduction in capacity compared with lower rates and the cycling stability remains excellent. These results indicate the stability of the **NaFP** crystal structure and the reversible nature of Na^+ ion insertion. In order to verify the retention of the structural integrity after electrochemical cycling *ex situ* powder XRD was performed on materials obtained at the end of discharge and subsequent recharge (SI, Fig. S7). This confirmed that the structure of **NaFP** is stable on sodium insertion/extraction. The three-dimensional interconnected channel system of the crystal structure promotes the Na^+ diffusion, avoiding blockage and promoting the excellent capacity retention and good cycling stability observed.

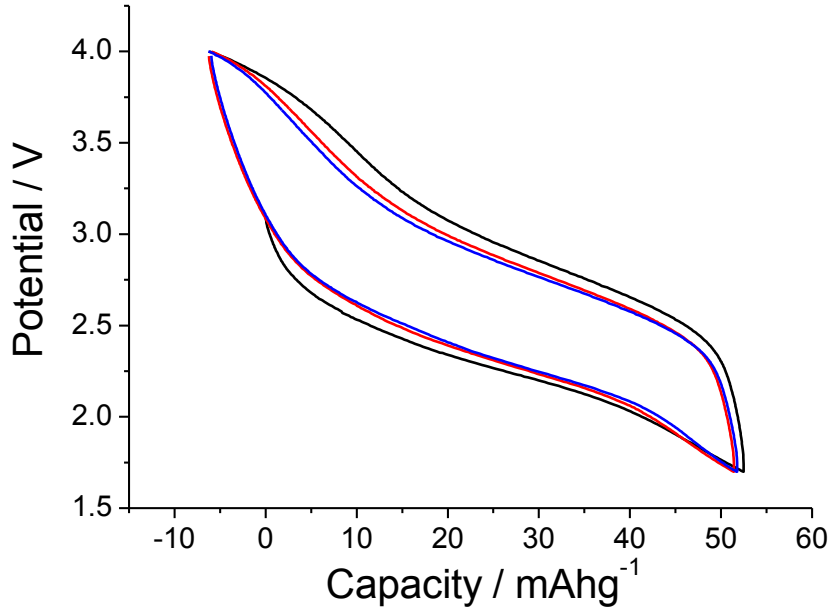

Fig. 6. Load curves at a rate of C/10 (10mA/g) and a potential range 1.7-4 V (cycle 1 - black, cycle 2 –red, cycle 3 – blue).

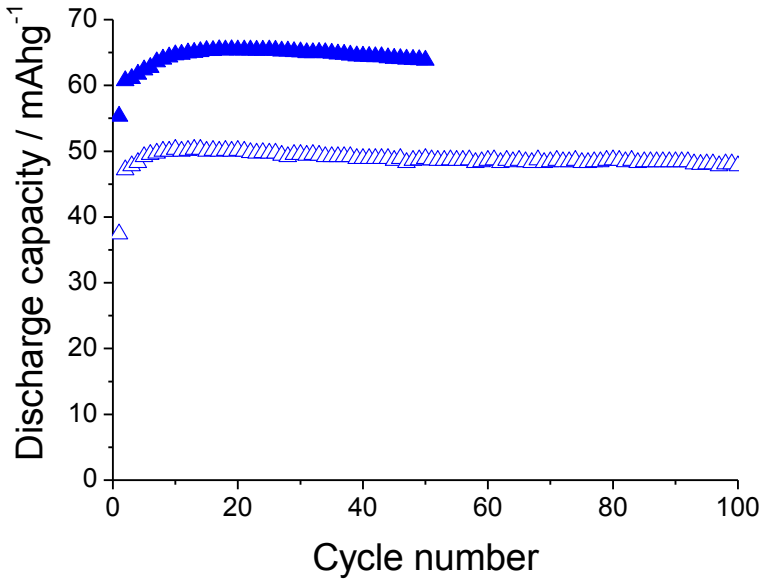

Fig. 7. Discharge capacity vs. cycle number for **NaFP** at a rate of C/10 (filled triangles) and at a rate of 1C (open triangles) over the potential window 1.7-4.0 V).

Physical properties. From the point of view of magnetic topology **NaFP** is characterized by a non-trivial magnetic sublattice with two different magnetic subsystems corresponding to the two crystallographic sites for Fe^{3+}, as described above (Fig. 5). Thermodynamic properties of **NaFP** indicate formation of a magnetically ordered state at T_C = 9.4 K. As seen in the upper panel of Fig. 8, on cooling the dc magnetic susceptibility, χ, increases proportionally to inverse temperature, exhibiting a sharp upturn at T_C = 9.4 K. Approximation of the high temperature magnetic susceptibility by a Curie – Weiss law: $\chi = \chi_0 + C/(T-\Theta)$ allows estimation of the temperature-independent term $\chi_0 = -2.3 \cdot 10^{-5}$ emu/mol, Curie constant C = 13.47 emu K/mol and Weiss temperature Θ = – 21 K. These parameters have been used for the linear fit of $1/(\chi - \chi_0)$ vs. T, shown by solid line in the upper panel (Fig. 8). The appearance of spontaneous magnetization at T_C (enlarged in the Inset to upper panel of Fig. 8) may be a signature of a ferrimagnetic ground state stabilized by the competition of various antiferromagnetic exchange interactions. This spontaneous moment amounts to about 1/3 of the total magnetization, as shown in the upper inset to Fig.8.

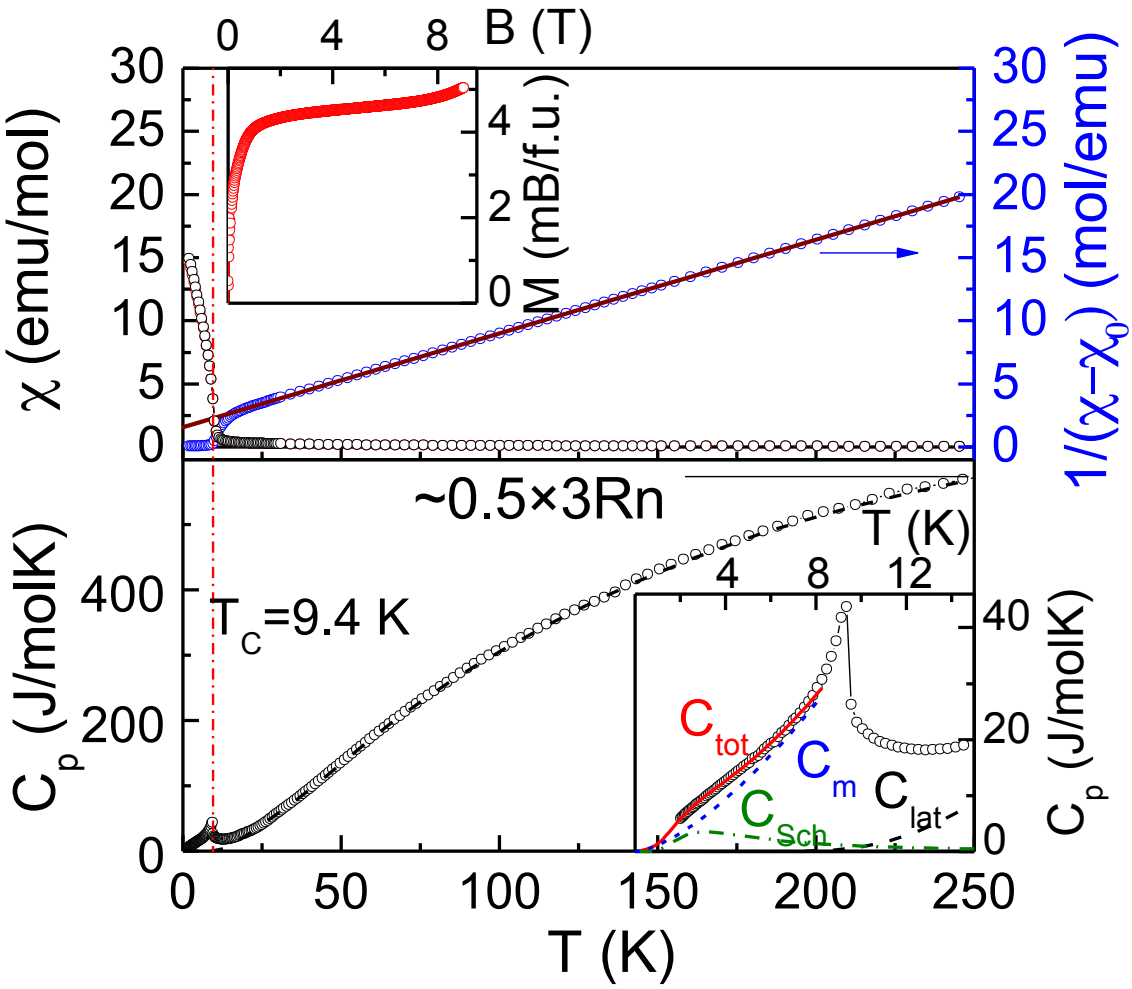

Fig. 8. Thermodynamic properties of **NaFP**. Upper panel represents dc-magnetic susceptibility taken at B = 0.1 T and lower panel represents specific heat. Upper panel contains inset with magnetization curve measured at 2 K. Lower panel contains inset with enlarged low temperature region with maximum at the magnetic phase transition at T_C = 9.4 K.

The Curie constant *C* is proportional to the number of magnetic ions, *n*, via the expression $C = ng^2S(S+1)\mu_B^2N_A/3k_B$, where μ_B, N_A, k_B are Bohr, Avogadro and Boltzmann constants. The effective magnetic moment obtained from the above *C* value (μ_{eff} = 10.38 μ_B) compares well with the theoretical estimation according to the formula $\mu_{theor}^2 = ng^2S(S+1)\mu_B^2$. This results in $\mu_{theor} \approx 10.22\ \mu_B$ for three high-spin $S = 5/2$ Fe^{3+} ions per formula unit with average value g = 1.993±0.003 obtained directly from the ESR study, as described below.

The specific heat C_p demonstrates a broad shoulder at low temperatures, λ - type anomaly at T_C and at room temperature reaches approximately half of Dulong – Petit thermodynamic limit $3NR$ = 1247.5 J/mol K (for N = 50 atoms per formula unit) at room

temperature, as shown by horizontal line in the lower panel of Fig. 8. This points to a rather high Debye temperature in the system presumably due to the presence of many light atoms in the structure. A rough estimation of lattice contribution C_{lat} was carried out by fitting the $C_p(T)$ dependence by three Einstein functions, shown by dotted lines in lower panel of Fig. 8. The lattice contribution seems to be negligibly small at $T < T_C$. Therefore, the low temperature values of Cp were fitted by the sum of a Schottky type anomaly C_{Sch} and a magnetic term C_m shown by dash-dotted and short dashed lines in the inset to the lower panel of Fig. 8. The Schottky type anomaly is probably due to the Zeeman splitting of five Fe^{3+} (S = 5/2) levels in the presence of the internal magnetic field induced at $T < T_C$. The energy gap for this Schottky type anomaly is estimated as Δ = 7.5 K. The magnetic contribution is proportional to $T^{3/2}$, which is typical for ferro/ferrimagnets.

ESR data corroborate very well with the picture derived from the structural and thermodynamic data. Evolution of the X-band ESR spectra with temperature is shown in the SI (Fig. S8). At high temperature the whole spectrum is dominated by an absorption line of Lorentzian line shape indicative of exchange narrowing, which is typical for magnetically concentrated systems. Nevertheless, an accurate quantitative analysis of the lineshape requires the use of a sum of two Lorentzian functions. This means that two different resonance modes L_1 and L_2 may be distinguished in the spectrum, which may be attributed to the signals from the two crystallographically-distinct Fe^{3+} sites. Temperature dependences of the effective g-factor, the ESR linewidth and the integral ESR intensity for the resolved components of ESR spectra as derived from the fitting by a sum of two Lorentzian functions are collected in Fig. 9.

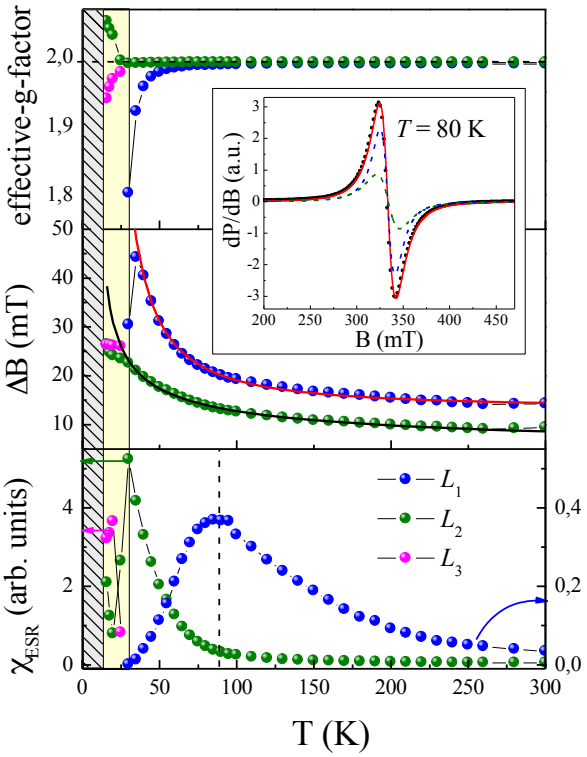

Fig. 9. The temperature dependences of the effective g-factor (upper panel), the ESR linewidth (middle panel) and the integral ESR intensity (lower panel) for three resolved components L_1, L_2 and L_3 of the ESR spectra. The inset shows a representative example of the ESR spectrum decomposition along with two different resonance modes, which are shown by colored dashed lines, while their sum is shown by the red solid line.

At high temperatures both resonance modes are characterized by isotropic effective g-factors $g_1 = 1.99(1)$ and $g_2 = 1.99(3)$, which are typical of high spin Fe^{3+} (S = 5/2) in octahedral oxygen coordination. Upon decreasing the temperature the resonance field of the L_1 line increases, indicating development of short-range correlations. At the same time the resonance field of L_2 line remains almost constant down to lower temperature and shows a visible shift only in the immediate proximity to T_C (upper panel in Fig. 9). The difference in origin of the two resonance modes is most obvious from the behavior of the integral ESR intensity χ_{ESR}, which is proportional to the number of magnetic spins (lower panel in Fig. 9). The integral ESR intensity χ_{ESR2} for the L_2 mode demonstrates Curie-Weiss-like behavior down to ~30 K, then passes through a maximum and decreases non-monotonically. In contrast χ_{ESR1} passes through a broad maximum at about 90 K resembling the behavior of a low-dimensional spin-gapped system. Taking into account that the Fe(2) ions form alternating chains coupled via two phosphite groups one can expect that the L_1 mode corresponds to the signal from the Fe(2) magnetic sublattice, while the L_2 mode can be related to the signal from Fe(1) ions, which are more weakly linked magnetically (Fig. 4) and bridge the chains into a 3D magnetic network. At $T^* \sim 30$ K the L_1 signal vanishes and cannot be detected at $T < T^*$. Instead, at lower temperature, another resonance mode L_3 is observed, being related tentatively to the presence of a small amount of paramagnetic impurity, for instance, isolated Fe^{3+} ions.

The ESR linewidth (middle panel in Fig. 9) shows similar behavior for both resolved L_1 and L_2 components: it remains almost constant at high temperatures, then demonstrates a rapid increase as temperature decreases, most pronounced at temperatures below 100 K. Such broadening of exchange-narrowed ESR lines has often been observed for various antiferromagnetic systems,[38-43] and has been explained in terms of critical behavior of the ESR linewidth due to slowing down of spin fluctuations as the critical temperature is approached from above.[44-47]

In this case, the broadening of ESR line can be accounted by Huber's formula

$$\Delta B(T) = \Delta B^* + A \cdot \left[\frac{T_N^{ESR}}{T - T_N^{ESR}} \right]^{\beta} \qquad (1)$$

where ΔB denotes the ESR linewidth, ΔB^* is the limiting high-temperature value of the linewidth, A is an empirical parameter, $T^{ESR}{}_N$ is the temperature of the order-disorder transition and β is the critical exponent. Solid red and black lines on the middle panel of Fig.

9 represent a least squares fitting of experimental data according to Eq. (1) for L_1 and L_2 modes, respectively. The fact that a noticeable broadening occurs already at temperatures around 100 K, i.e., 10 times higher than the magnetic ordering temperature, points to appreciable magnetic fluctuations at elevated temperatures. The best description of experimental data has been achieved with the model parameters ΔB^*_1 = 133 mT, T^{ESR}_{N1} = 9.75 K, β_1 = 1.4 and ΔB^*_2 = 30 mT, T^{ESR}_{N2} = 9.89 K, β_2 = 0.47 for L_1 and L_2 modes, respectively. It can be seen that despite the different T-range for fitting the estimated values of T^{ESR}_N are almost identical for both modes and compare well with T_C obtained from both dc/ac magnetic susceptibility and specific heat. At the same time the critical exponents take rather different values for L_1 and L_2 modes highlighting the rather different character of magnetic correlations for the two magnetic sublattices.

In the frame of the Kawasaki approach[44,45] the critical exponent can be expressed as $\beta = -[1/2(7+\eta)\nu-2(1-\alpha)]$ where ν describes the divergence of correlation length, η is a critical exponent for the divergence of static correlations and α reflects the divergence of the specific heat. In the framework of the Heisenberg model the values are $\eta = \zeta = 0$ and $\nu = 2/3$ for 3D antiferromagnets[44,45] leading to $\beta = 1/3$. In the case of magnetic systems with lower dimensionality, the critical exponent is expressed as $\beta = (3 - 2\eta)\nu$ and $(3.5 - 2\eta)\nu$ for 2D and 1D systems respectively.[48,49] Hence, the corresponding values β using the values $\eta = 0$ and $\nu = 1/2$[48] should result in $\beta = 3/2$ and 7/4 for 2D and 1D systems respectively. Obviously, the present result evidences a 3D character of magnetic fluctuations for the L_2 mode ($\beta_2 = 0.47$) but low dimensional behavior for the L_1 mode ($\beta_1 = 1.4$).

Conclusions

A novel iron fluoro-phosphite, $NaFe_3(HPO_3)_2((H,F)PO_2OH)_6$, has been synthesized by a dry low temperature synthesis route. The phase has been shown to be electrochemically active for reversible intercalation of Na^+ ions, with an average discharge voltage of 3V and an experimental capacity of 60 mAh/g. The simple synthesis, low cost materials, excellent capacity retention and efficiency of this cathode material could find applications in the next generation of Na-battery systems.

The title compound also shows unusual magnetic properties. Its magnetic subsystem, represented by Fe^{3+} ions in two crystallographically inequivalent positions in a triangular arrangement, exhibits both three-dimensional and one-dimensional trends in the paramagnetic state ($T > T_C$) and spontaneous magnetization in the magnetically ordered state ($T < T_C$). A fuller investigation of the ferrimagnetic properties of this compound, using both microscopic and macroscopic physical tools, together with theoretical modelling, is underway, and will be published in a separate publication.

Supporting Information

Powder XRD of as-made and electrochemically-cycled material, single crystal XRD in CIF format, and ESR spectra versus *T*. This material is available free of charge via the Internet at http://pubs.acs.org. Crystallographic details (CIF format) for the single crystal study have been deposited with the ICSD (deposition number 430570). Other pertinent raw data supporting this publication are available at web address to follow.

Corresponding authors:

E-mail #vasil@mig.phys.msu.ru, *pl@st-andrews.ac.uk

Acknowledgements

Prof. A. M. S. Slawin and David Price are thanked for experimental assistance. We thank the University of St Andrews and EPSRC (EP/K503162/1) for partial support of a studentship to I.M. The work was supported by the RFBR (grants 14-02-00245, 14-02-00111. The Russian team acknowledge support from the Ministry of Education and Science of the Russian Federation in the framework Increase Competitiveness Program of NUST «MISiS» (№ K4-2015-020 and K2-2015-075) and by Act 211 Government of the Russian Federation, contract(№ 02.A03.21.0006).

References

1. Kim, S.W.; Seo, D.H.; Ma, X.; Ceder, G.; Kang, K. Electrode Materials for Rechargeable Sodium-Ion Batteries: Potential Alternatives to Current Lithium-Ion Batteries. *Adv. Energy Mater.* **2012**, *2*, 710-721.
2. Pan, H.; Hu, Y.S.; Chen, L. Room-temperature stationary sodium-ion batteries for large-scale electric energy storage. *Energy Environ. Sci.* **2013**, *6*, 2338-2360.
3. Slater, M.D.; Kim, D.; Lee, E.; Johnson, C.S. Sodium-Ion Batteries. *Adv. Funct. Mater.* **2013**, *23*, 947-958.
4. Yabuuchi, N.; Kubota, K.; Dahbi, M.; Komaba, S. Research Development on Sodium-Ion Batteries. *Chem. Rev.* **2014**, *114*, 11636-11682.
5. Palomares, V.; Casas-Cabanas, M.; Castillo-Martínez, E.; Han, M.H.; Rojo, T. Update on Na-based battery materials. A growing research path. *Energy Environ. Sci.* **2013**, *6*, 2312-2337.
6. Palomares, V.; Serras, P.; Villaluenga, I.; Hueso, K.B.; Carretero-González, J.; Rojo, T. Na-ion batteries, recent advances and present challenges to become low cost energy storage systems. *Energy Environ. Sci.* **2012**, *5*, 5884-5901.
7. Dahbi, M. ; Yabuuchi, N.; Kubota, K. ; Tokiwa, K. ; Komaba, S. Cypress leaf-like Sb as anode material for high-performance sodium-ion batteries. *Phys. Chem. Chem. Phys.* **2014**, *16*, 15007-15028.
8. Masquelier, C. ; Croguennec, L. Polyanionic (Phosphates, Silicates, Sulfates) Frameworks as Electrode Materials for Rechargeable Li (or Na) Batteries. *Chem. Rev.* **2013**, *113*, 6552-6591.

9. Komaba, S.; Murata, W.; Ishikawa, T.; Yabuuchi, N.; Ozeki, T.; Nakayama, T.; Ogata, A.; Gotoh, K.; Fujiwara, K. Electrochemical Na Insertion and Solid Electrolyte Interphase for Hard-Carbon Electrodes and Application to Na-Ion Batteries. *Advanced Functional Materials* **2011**, *21*, 3859-3867.
10. Mortemard de Boisse, B. ; Carlier, D. ; Guignard, M. ; Delmas, C. Structural and Electrochemical Characterizations of P2 and New O3-$Na_xMn_{1-y}Fe_yO_2$ Phases Prepared by Auto-Combustion Synthesis for Na-Ion Batteries. *J. Electrochem.Soc.* **2013**, *160*, A569-A574.
11. Yabuuchi, N.; Yoshida, H.; Komaba, S. Crystal Structures and Electrode Performance of Alpha-$NaFeO_2$ for Rechargeable Sodium Batteries. *Electrochemistry* **2012**, *80*, 716-719.
12. Komaba, S.; Takei, C.; Nakayama, T.; Ogata A.; Yabuuchi, N. Electrochemical intercalation activity of layered $NaCrO_2$ vs. $LiCrO_2$. *Electrochem. Commun.* **2010**, *12*, 355-358.
13. Ma, X.; Chen, H.; Ceder, G. Electrochemical Properties of Monoclinic $NaMnO_2$ Batteries and Energy Storage. *J. Electrochem. Soc.* **2011**, *158*, A1307-A1312.
14. Mendiboure, A.; Delmas, C.; Hagenmuller, P. Electrochemical intercalation and deintercalation of Na_xMnO_2 bronzes. *J. Solid State Chem.* **1985**, *57*, 323-331.
15. Caballero, A. ; Hernan, L. ; Morales, J. ; Sanchez, L. ; Santos Pena, J. ; Aranda, M.A.G. Synthesis and characterization of high-temperature hexagonal P2-$Na_{0.6}MnO_2$ and its electrochemical behaviour as cathode in sodium cells. *J. Mater. Chem.*, **2002**, *12*, 1142-1147.
16. Su, D.; Wang, C.; Ahn, H.J.; Wang, G. Single Crystalline $Na_{0.7}MnO_2$ Nanoplates as Cathode Materials for Sodium-Ion Batteries with Enhanced Performance. *Chem. Eur. J.* **2013**, *19*, 10884-10889.
17. Billaud, J.; Singh, G.; Armstrong, A.R.; Gonzalo, E.; Roddatis, V.; Armand, M.; Rojo, T.; Bruce, P.G. $Na_{0.67}Mn_{1-x}Mg_xO_2$ ($0 \leq x \leq 0.2$): a high capacity cathode for sodium-ion batteries. *Energy Environ. Sci.* **2014**, *7*, 1387-1391.
18. Yabuuchi, N.; Kajiyama, M.; Iwatate, J.; Nishikawa, H.; Hitomi, S.; Okuyama, R.; Usui, R.; Yamada, Y.; Komaba, S. P2-type $Na_x[Fe_{1/2}Mn_{1/2}]O_2$ made from earth-abundant elements for rechargeable Na batteries. *Nature Mater.* **2012**, *11*, 512-517.
19. Ellis, B.; Lee, K. T.; Nazar, L. F. Positive Electrode Materials for Li-Ion and Li-Batteries. *Chem. Mater.* **2010**, *22*, 691-714.
20. Padhi, A. K.; Manivannan, V.; Goodenough, J. B. Tuning the Position of the Redox Couples in Materials with NASICON Structure by Anionic Substitution. *J. Electrochem. Soc.* **1998**, *145*, 1518-1520.
21. Murugavel, R.; Choudhury, A.; Walawalkar, M. G.; Pothiraja, R.; Rao, C.N.R. Metal Complexes of Organophosphate Esters and Open-Framework Metal Phosphates: Synthesis, Structure, Transformations, and Applications. *Chem. Rev.* **2008**, *108*, 3549-3655.
22. Padhi, A. K.; Nanjundaswamy, K. S.; Goodenough, J.B. Phospho-olivines as Positive-Electrode Materials for Rechargeable Lithium Batteries. *J. Electrochem. Soc.* **1997**, *144*, 1188-1194.
23. Anji Reddy, M.; Pralong, V.; Caignaert, V.; Varadaraju, U. V.; Raveau, B. Monoclinic iron hydroxy sulphate: A new route to electrode materials. *Electrochem. Commun.* **2009**, *11*, 1807-1810.

24. Recham, N.; Chotard, J.N.; Dupont, L.; Delacourt, C.; Walker, W.; Armand, M.; Tarascon, J.M. A 3.6 V lithium-based fluorosulphate insertion positive electrode for lithium-ion batteries . *Nature Mater.* **2010**, *9*, 68-74.
25. Rousse, G.; Tarascon, J.M. Sulfate-Based Polyanionic Compounds for Li-Ion Batteries: Synthesis, Crystal Chemistry, and Electrochemistry Aspects. *Chem. Mater.* **2014**, *26*, 394-406.
26. Nytén, A.; Abouimrane, A.; Armand, M.; Gustafsson, T.; Thomas, J.O. Electrochemical performance of Li_2FeSiO_4 as a new Li-battery cathode material. *Electrochem. Commun.* **2005**, *7*, 156-160.
27. Islam, M.S.; Dominko, R.; Masquelier, C.; Sirisopanaporn, C.; Armstrong, A. R.; Bruce, P.G. Silicate cathodes for lithium batteries: alternatives to phosphates? *J. Mater. Chem.* **2011**, *21*, 9811-9818.
28. Legagneur, V.; An, Y.; Mosbah, A.; Portal, R.; Le Gal La Salle, A.; Verbaere, A.; Guyomard, D.; Piffard, Y. $LiMBO_3$ (M=Mn, Fe, Co): synthesis, crystal structure and lithium deinsertion/insertion properties. *Solid State Ionics* **2000**, *139*, 37-46.
29. Yamada, A.; Iwane, N.; Harada, Y.; Nishimura, Sh.-I; Koyama, Y.; Tanaka, I. Lithium Iron Borates as High-Capacity Battery Electrodes. *Adv. Mater.* **2010**, *22*, 3583-3587.
30. Chen, H.; Hautier, G.; Ceder, G. Synthesis, Computed Stability, and Crystal Structure of a New Family of Inorganic Compounds: Carbonophosphates. *J. Am. Chem. Soc.* **2012**, *134*, 19619-19627.
31. Chen, H.; Hao, Q.; Zivkovic, O.; Hautier, G.; Du, L.; Tang, Y.; Hu, Y.; Ma, X.; Grey, C. P.; Ceder, G. Sidorenkite ($Na_3MnPO_4CO_3$): A New Intercalation Cathode Material for Na-Ion Batteries. *Chem. Mater.* **2013**, *25*, 2777-2786.
32. Chung, U.; Mesa, J. L.; Pizarro, J. L.; De Meatza, I.; Bengoechea, M.; Fernandez, J. R.; Arriortua, M. I.; Rojo, T. $Li_{1.43}[Fe^{II}_{4.43}Fe^{III}_{0.57}(HPO_3)_6]\cdot 1.5H_2O$: A Phosphite Oxoanion-Based Compound with Lithium Exchange Capability and Spin-Glass Magnetic Behavior. *Chem. Mater.* **2011**, *23*, 4317-4330.
33. YaghoobnejadAsl, H.; Choudhury, A. Phosphite as Polyanion-Based Cathode for Li-Ion Battery: Synthesis, Structure, and Electrochemistry of $LiFe(HPO_3)_2$. *Inorg. Chem.* **2015**, *54*, 6566-6572.
34. YaghoobnejadAsl, H.; Ghosh, K.; Meza, M. P. V.; Choudhury, A. $Li_3Fe_2(HPO_3)_3Cl$: an electroactive iron phosphite as a new polyanionic cathode material for Li-ion battery. *J. Mater. Chem. A* **2015**, *3*, 7488-7497.
35. Brese, N. E.; O'Keeffe, M. Bond-valence parameters for solids. *Acta Crystallogr.B.* **1991**, *47*, 192-197.
36. Loub, J. Crystal chemistry of inorganic phosphites. *Acta Crystallogr.B.* **1991**, *47*, 468-473.
37. Nava-Avendano, J.; Arroyo-de Dompablo, M.E.; Frontera, C.; Ayllón, J.A.; Palacín, M.R. Study of sodium manganese fluorides as positive electrodes for Na-ion batteries. *Solid State Ionics*, **2015**, *278*, 106-113.
38. Causa, M.T.; Tovar, M.; Obradors, X. ; Labarta, A. ; Tejada, Electron-spin resonance in the spin-glass-like system $Fe_{1-x}Ga_xSbO_4$. *J. Phys. Rev. B*, **1991**, *44*, 4455-4460.
39. Oseroff, S.; Calvo, R.; Giriat, W. Electron spin resonance in $Cd_{1-x}Mn_xTe$. *J. Appl. Phys.* **1979**, *50*, 7738.

40. Wolter, A.U.B.; Lipps, F.; Schäpers, M.; Drechsler, S.L.; Nishimoto, S.; Vogel, R.; Kataev, V.; Büchner, B.; Rosner, H.; Schmitt, M.; Uhlarz, M.; Skourski, Y.; Wosnitza, J.; Süllow, S.; Rule, K.C. Magnetic properties and exchange integrals of the frustrated chain cuprate linarite $PbCuSO_4(OH)_2$. *Phys. Rev. B* **2012**, *85*, 014407-1-16.
41. Zvereva, E.A. Savelieva, O.A.; Titov, J.D.; Evstigneeva, M.A.; Nalbandyan, V.B.; Kao, C.N.; Lin, J.Y.; Presniakov, I.A.; Sobolev, A.V.; Ibragimov, S.A.; Abdel-Hafiez, M.; Krupskaya, Yu.; Jähne, C.; Tan, G.; Klingeler, R.; Büchner, B.; Vasiliev, A.N. A new layered triangular antiferromagnet Li_4FeSbO_6: spin order, field-induced transitions and anomalous critical behavior. *Dalton Trans.*, **2013**, *42*, 1550-1566.
42. Zvereva, E.A.; Evstigneeva, M.A.; Nalbandyan, V.B.; Savelieva, O.A.; Ibragimov, S.A.; Volkova, O.S.; Medvedeva, L.I.; Vasiliev, A.N.; Klingeler, R.; Büchner, B. Monoclinic honeycomb-layered compound $Li_3Ni_2SbO_6$: preparation, crystal structure and magnetic properties. *Dalton Trans.*, **2012**, *41*, 572-580.
43. Zvereva, E.A.; Stratan, M.I.; Ovchenkov, Y.A.; Nalbandyan, V.B.; Lin, J.Y.; Vavilova, E.L.; Iakovleva, M.F.; Abdel-Hafiez, M.; Silhanek, A.V.; Chen, X.J.; Stroppa, A.; Picozzi, S.; Jeschke, H.O.; Valentí, R.; Vasiliev, A.N. Zigzag antiferromagnetic quantum ground state in monoclinic honeycomb lattice antimonates $A_3Ni_2SbO_6$ (A = Li, Na). *Phys. Rev. B*, **2015**, *92*, 144401-1-12.
44. Kawasaki, K. Anomalous spin relaxation near the magnetic transition. *Prog. Theor. Phys.*, **1968**, *39*, 285-311.
45. Kawasaki, K. Ultrasonic attenuation and ESR linewidth near magnetic critical points. *Phys. Lett. A*, **1968**, *26*, 543.
46. Mori, H.; Kawasaki, K. Antiferromagnetic Resonance Absorption. *Progr. Theor. Phys.*, **1962**, *28*, 971-987.
47. Huber, D.L. Critical-Point Anomalies in the Electron-Paramagnetic-Resonance Linewidth and in the Zero-Field Relaxation Time of Antiferromagnets. *Phys. Rev. B*, **1972**, *6*, 3180-3186.
48. Richards, P.M. Critical exponents for NMR and ESR linewidths in a two-dimensional antiferromagnet. *Solid State Commun.*, **1973**, *13*, 253-256.
49. Anders, A.G.; Volotski, S.V. EPR in 1-d and 2-d antiferromagnetic systems. *J. Magn. Magn. Mater.*, **1983**, *31-34*,1169-1170.

For Table of Contents only

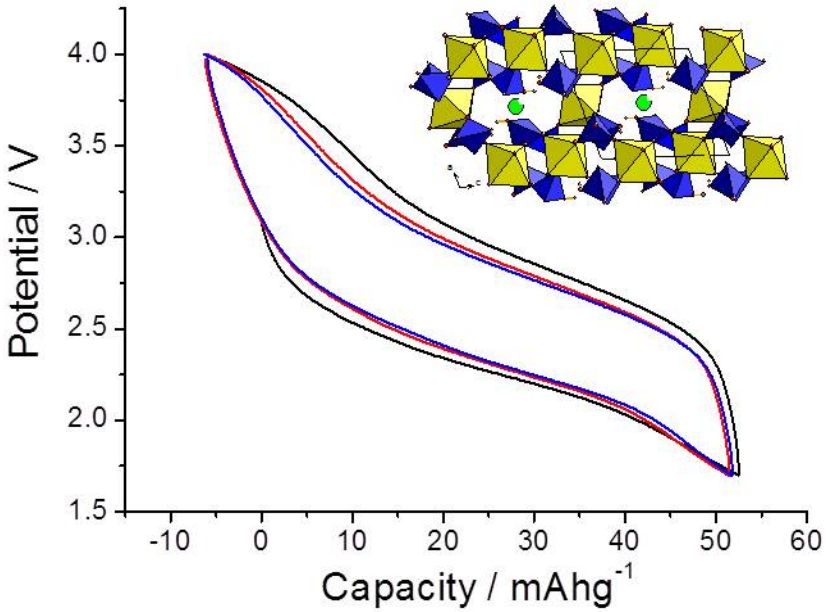

Synopsis

The title compound shows reversible intercalation of Na^+ ions, with an average discharge voltage of 2.5 V and an experimental capacity of up to 90 mAh/g. It also exhibits ferrimagnetic ordering at 9.4 K.